Ocean Engineering 172 (2019) 684–696

Contents lists available at ScienceDirect

Ocean Engineering

journal homepage: www.elsevier.com/locate/oceaneng

Model investigations of discharge plumes generated by deep-sea nodule mining operations

Andrew J. Rzeznik[a,*], Glenn R. Flierl[b], Thomas Peacock[b]

[a] DMC Inc., Somerville, MA, 02144, USA
[b] Massachusetts Institute of Technology, Cambridge, MA, 02139, USA

ARTICLE INFO

Keywords:
Deep-sea nodule mining
Sediment plumes
Ambient stratification
Background shear
Compressibility effects

ABSTRACT

Deep-sea nodule mining operations potentially involve plans for discharge plumes to be released into the water column by surface operation vessels. As such, we consider the effects of non-uniform, realistic stratifications with vertical shear on forced compressible plumes for application to nodule mining applications. The plume model is developed to account for the influence of thermal conduction through the discharge pipe and an initial adjustment phase. We investigate and elucidate the substantial role of compressibility, for which a dimensionless number is introduced to determine its importance compared to that of the background stratification. Our results show that (i) small-scale stratification features can have a significant impact, (ii) in a static ambient there is a discharge flow rate that minimizes the plume vertical extent, (iii) the ambient velocity profile plays an important role in determining final plume scale and dilution factor, and (iv) for a typical plume the dilution factor is expected to be several hundred to a thousand.

1. Introduction

There has been a resurgence of interest in the potential of seabed mining operations to exploit deposits of mineral resources that lie in the deep ocean, the three most commonly proposed being seafloor massive sulfides, ferromanganese crusts and polymetallic (manganese) nodules (Boschen et al., 2013; Hein and Koschinsky, 2014). Though the proposed mining methods vary substantially in several aspects, there are also some commonalities. A seafloor based mining apparatus collects mineral ores and some amount of unwanted sediment, and this mixture is transported via a riser to a tethered surface vessel for initial processing before being shipped to land-based processing facilities. In order to avoid extensive shipping of sediment by-products, it is to be considered whether commercially undesirable sediment and any other by-products of the surface treatment process can thereafter be released into the water column via a return pipe as a discharge plume, with the ultimate goals being either deposition at the ocean bottom and/or environmentally acceptable levels of dilution within the water column (Assembly of Engineering, U.S., 1975).

Few studies have been performed regarding the form and properties of discharge plumes for nodule mining operations, which is the focus of this paper. The Deep Ocean Mining Effects Study (DOMES) (Lavelle et al., 1982; Burns, 1980) tracked a one-fifth commercial scale discharge, although rather than being released at depth the discharge occurred at the surface. Nawab and Luck (1979) presented echosounder data for a release discharged at a depth of 400 m, with the ensuing plume reaching down to 800 m. Numerical modeling of long-time transport of sediment released in a discharge plume in the Pacific Ocean was performed by Segschneider and Sndermann (1998) and Rolinski et al. (2001), using a large-scale ocean transport model combined with a Lagrangian transport model; the nature of the discharge plume itself, however, was not considered.

If returning all sediment back down to the seabed again is not an option (Collins et al., 2013), then consideration has been for a return pipe that extends to some intermediate depth in the water column (Oebius et al., 2001; Santo et al., 2013; Schriever and Thiel, 2013), with a generally accepted requirement that this be at least below the euphotic zone to ensure that suspended sediment does not impede photosynthetic activity. For such plumes, the initial diameter, release depth, water temperature, sediment concentration, the nature of the background stratification, and the ambient velocity structure all influence the characteristics of the resulting plume and the fate of the sediment within. Though in principle the multiphase nature of the suspension could influence the plume dynamics, as will be demonstrated later a highly reasonable first approximation is that until the very final stages of its downward evolution (at which point the turbulent velocities become small enough that sedimentation, coagulation and flocculation are significant processes) the discharge plume can be viewed as

* Corresponding author.
E-mail address: andrew.rzeznik@dmcinfo.com (A.J. Rzeznik).

https://doi.org/10.1016/j.oceaneng.2018.12.012
Received 23 June 2018; Received in revised form 28 September 2018; Accepted 5 December 2018
0029-8018/ © 2018 Elsevier Ltd. All rights reserved.

a downward release of negatively buoyant fluid with initial momentum in a stably-stratified background environment (Droppo, 2006).

The relevant plume theory can trace its origins to the classic turbulent plume model (Morton et al., 1956) in which a system of three equations is derived based on the principles of conservation of volume, momentum and buoyancy, furthermore assuming self-similarity and an entrainment coefficient. These equations can be modified with a cross flow term and supplemented with two positional equations to allow for tracking a plume released in an ambient velocity field (Devenish et al., 2010; wei Lee and Chu, 2003).

Initially, model plumes considered were simply point sources of buoyancy flux in space, but subsequent developments considered plumes that also initially have a momentum flux (Morton, 1958). It was shown that the initial nature of the plume can be characterized by a dimensionless ratio of the buoyancy and momentum flux, which allows efficient calculation of the plume height based on any initial conditions for either a zero or uniform stratification (Morton and Middleton, 2006). This ratio is referred to as the plume Richardson number (Hunt & van den Bremer, 2010),

$$\mathrm{Ri} = \frac{g'b}{U^2}, \tag{1}$$

where U is a characteristic vertical velocity in the plume, b is a characteristic radius, and $g' = g(\Delta\rho)/\rho_a$ is the reduced gravity; here g is gravity, $\Delta\rho$ is the density difference of the plume compared to the surrounding ambient, and ρ_a is the ambient fluid density. For $\mathrm{Ri} \ll 1$, momentum dominates and this is called the "forced" plume regime, whereas $\mathrm{Ri} \gg 1$ implies either very large buoyancy or plume radius for the given velocity and this is termed a "lazy" plume (Hunt and Kaye, 2005). In both cases, the local Richardson number along the length of a plume tends to approach an order one constant (based on problem scaling), causing both forced and lazy plumes to converge to the same attracting solution at long distances from the source. However, the local dynamics near the source can be very different for $\mathrm{Ri} \ll 1$ or $\mathrm{Ri} \gg 1$. In particular, for a lazy plume it has been shown that the entrainment parameter can no longer be considered a constant, and instead its value changes near the plume's source based on the specific value of the Richardson number (Hunt & van den Bremer, 2010; Matulka et al., 2014). For a uniform incompressible ambient, the initial Richardson number of the plume completely determines the dynamics of the problem. In many relevant problems in environmental dynamics, however, the background density stratification is nonuniform, and the interplay between the specific form of the stratification and the initial conditions creates more involved dynamics (Kaye, 2008; Woods, 2010).

The different phases in the lifetime of such a downwards plume are as follows. For any finite source plume there exists an initial zone of flow establishment (ZFE) during which the flow is not self-similar, and the reduced ordinary differential equation model does not apply (Morton, 1958). This initial regime must be dealt with using different methods (Henderson-Sellers, 1983), after which a self similar profile is formed with the newly calculated initial data. As it descends, the plume entrains ambient fluid until it reaches a level of neutral buoyancy, after which its remaining momentum carries it a finite distance farther as the buoyancy flux now becomes positive; the momentum eventually reaches zero and the plume rebounds because of the now positive buoyancy. Thereafter, this is followed by an intrusion of the plume fluid outward at the neutral buoyancy level (Mehaddi et al., 2013). The process of rebound followed by horizontal intrusion is termed "trapping", since the material in the plume becomes trapped at a particular depth in the water column; this is as opposed to a free plume, which continues to extend indefinitely until it reaches a solid boundary. Complications to this basic picture can arise when enough suspended sediment is present to act as a separate phase; In such a situation it is possible for the plume phases to split, with the trapping levels modified due to the sudden loss or gain in buoyancy (Socolofsky and Adams, 2002).

If the stratification is non-constant, a plume may or may not be trapped at a finite depth, depending on the local density gradient. It has been shown that when the stratification is given by a power law, the critical exponent that separates trapped as opposed to free plumes is $-8/3$ (Caulfield and Woods, 1998), with plumes in slower-decaying stratifications becoming trapped at a finite depth. Even for the same net change in background density over a given vertical extent, the local form of the density gradient can determine whether or not a plume passes through that region or becomes trapped within it and ultimately forms an intrusion in the water column (Camassa et al., 2016). Typically, ocean stratifications show clear and pronounced non-linearity, which must be taken into account for the realistic modeling of a discharge plume. Further complications in modeling also arise due to the compressibility of ocean water at great depths and the multi-phase nature of the suspended particles in the plume (Bush et al., 2003), although we determine that the latter will only become a factor at the very deepest extent of a discharge plume.

In this paper, for application to deep-sea mining activities, we consider the general case of compressible plumes in non-uniform stratification with background vertical shear, focusing on the region of parameter space that is expected to be relevant to operations for nodule mining. We begin, in section 2, by presenting an overview of the equations for a compressible plume in a background stratification, introducing a dedicated parameter to identify the significance of compressibility. Since dimensional analysis methods used for uniform stratification are not so insightful for non-constant frequency, in section 3 we turn to numerical techniques to examine discharge plume characteristics as a function of the background stratification and plume initial conditions based on reasonable parameter values drawn from the literature, highlighting the effects of compressibility on the plume dimensions. Finally, we present a discussion and our conclusions in section 4.

2. Plume model

2.1. Axisymmetric model equations

Our axisymmetric model is based on that of Morton et al. (1956) with a modification for an ambient crossflow (Devenish et al., 2010). An illustration of the plume geometry is presented in Fig. 1. The integral model formulation has been used and validated in past research (Fischer et al., 1979; List, 1982; Papanicolaou and List, 1988); a more modern derivation of these equations can be found in wei Lee and Chu (2003). The plume has a characteristic radius $b(z)$, vertical mean turbulent velocity $u(r, z)$, and mean density $\rho(r, z)$, with z and r being the vertical and radial coordinates, respectively (z is chosen to be downward positive); gravity g is present. The background stratification profile is $\rho_a(z)$, with appropriately calculated corresponding buoyancy frequency N (See section 2.3 regarding details about how N is calculated). Initial conditions at $z = 0$ are the plume density, ρ_i, the plume radius, b_i and the volume flux, Q_i, with ρ_0 being a reference density. The plume spreads as it increases in depth, the volume entrainment by the turbulent plume being encapsulated by the entrainment parameter, α, which in simple models is assumed to be constant but in general can be considered as a function of the plume's local volume, momentum, and buoyancy flux (Matulka et al., 2014).

Using the turbulent, Boussinesq plume approximation and assuming a linear equation of state, the equations for conservation of volume, momentum, and mass deficiency for an axisymmetric plume reduce to the following system of ODE's in the absence of a crossflow (Vallis, 2006):

$$\frac{dQ}{dz} = 2\alpha M^{1/2}, \tag{2}$$

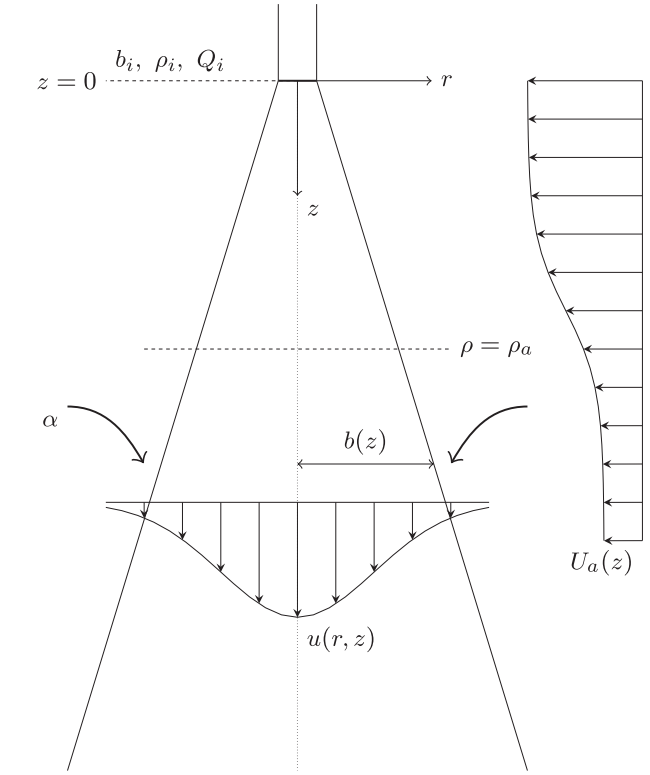


Fig. 1. A schematic illustrating the axisymmetric plume model. The plume begins at $z = 0$ with initial radius, b_i, density, ρ_i, and flow rate, Q_i. A background ambient cross flow $U_a(z)$ is also present. As the plume evolves downwards in the nonlinear background stratification ρ_a (see Fig. 2 for plot) the buoyancy flux reaches zero (i.e. $\rho = \rho_a$). The momentum of the plume causes it to continue downward until its momentum flux is zero (i.e. $u = 0$) at which point the plume will rebound (not illustrated).

$$\frac{dM}{dz} = \frac{QF}{M}, \tag{3}$$

$$\frac{dF}{dz} = -QN^2. \tag{4}$$

These equations are in terms of the volume flux $Q = \pi U b^2$, where $U(z)$ is the centerline velocity, momentum flux $M = \pi U^2 b^2$, and buoyancy flux $F = \pi U b^2 g \frac{\Delta\rho}{\rho_0}$. Depending on the vertical form of N^2, the above equations can then either be solved analytically or numerically for a given set of initial conditions.

These general plume equations can be modified to take into account refinements to the basic model. A variable λ is introduced to represent the ratio of the radii of the self similar density anomaly and velocity profiles (wei Lee and Chu, 2003). The equations for volume, momentum, and buoyancy flux variables can also be modified to account for Gaussian as opposed to tophat profiles (where the velocity is assumed to be constant for a finite radius and zero outside of that radius). These modifications can then be subsumed in a simple non-dimensionalization that allows for better understanding of the underlying physics. Taking F_0 as the initial buoyancy flux and introducing $N(z) = N_0 n(z)$, where $\max(n(z)) = 1$, one can introduce the following non-dimensional variables:

$$z = (F_0^{1/4} N_0^{-3/4})\tilde{z}, \tag{5}$$

$$Q = (4\alpha^2 F_0^{3/4} N_0^{-5/4})\tilde{q}, \tag{6}$$

$$M = (4\alpha^2 F_0 N_0^{-1})\tilde{m}, \tag{7}$$

$$F = (4\lambda\alpha^2 F_0)\tilde{f}\,. \tag{8}$$

Using these variables (and the results of Fox (1970) to reasonably assume $\lambda = 1$) the system of differential equations can be written as:

$$\frac{d\tilde{q}}{d\tilde{z}} = \tilde{m}^{1/2}, \tag{9}$$

$$\frac{d\tilde{m}}{d\tilde{z}} = \frac{\tilde{q}\tilde{f}}{\tilde{m}}, \tag{10}$$

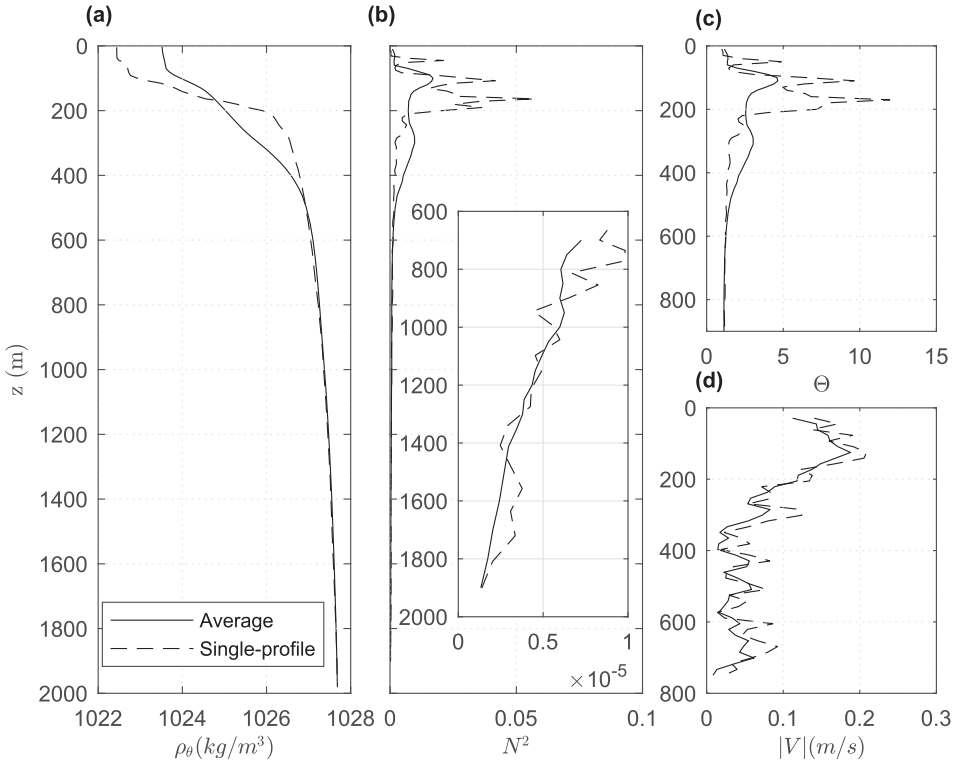


Fig. 2. The potential density and compressibility-modified density derivative along with ambient velocity for a specific and averaged ocean stratification. Fig. 2(a) shows the potential density for a single measured profile and an averaged profile, while Fig. 2(b) shows the corresponding compressible buoyancy frequency, as calculated using equation (27). Fig. 2(c) shows the non-dimensionalized compressibility number Θ for both profiles. The averaged profile is a 10 year average of July stratifications from the Roemmich-Gilson Argo Climatology. The single profile is an ARGO profile taken in the summer of 2016. All data are from 144 ± 1°W, 15 ± 1°N in the CCFZ. (d) Total absolute velocity profiles from ADCP data taken in the CCFZ. The averaged data averages 17 measured ADCP profiles. All data are from 132 ± 1°W, 11 ± 1°N in the CCFZ.

$$\frac{d\tilde{f}}{d\tilde{z}} = -n^2(\tilde{z})\tilde{w}. \tag{11}$$

Finally, one can define a non-dimensional radius, velocity, and buoyancy as follows:

$$\tilde{b} = \frac{\tilde{q}}{\tilde{m}^{1/2}}, \tag{12}$$

$$\tilde{u} = \frac{\tilde{m}}{\tilde{q}}, \tag{13}$$

$$\tilde{g} = \frac{\tilde{f}}{\tilde{q}}. \tag{14}$$

Solving equations (9)-(11) poses no issue numerically as the solution $\tilde{q}(\tilde{z})$, $\tilde{m}(\tilde{z})$, $\tilde{f}(\tilde{z})$ is finite given finite initial conditions. The same cannot be said of the radius, velocity, and buoyancy solutions $\tilde{b}(\tilde{z})$, $\tilde{u}(\tilde{z})$ and $\tilde{g}(\tilde{z})$ defined from equations (12)-(14). In particular, the plume radius $\tilde{b}(\tilde{z})$ tends to infinity at finite $\tilde{z}$. In reality, a continuous plume will first overshoot its level of neutral buoyancy before rebounding and then spreading out at the neutral buoyancy level. The total intrusion depth and the plume's width at this depth before it rebounds, however, may play a role in decision making (e.g. it is likely undesirable for a plume to reach the seabed with substantial momentum). We can report the plume's total depth as the maximum $\tilde{z}$ value, but the decrease of vertical velocity to zero at this depth poses issues for our single phase model, where low velocities may allow for phase separation via mass ejection of sediment and nodule fines, along with more general issues regarding near-zero denominators. As such, we report "end" plume parameters as corresponding to 90% of the calculated plume length.

A final modification must be performed to allow for ambient crossflows (Devenish et al., 2010). Standard plume models assume that the deformation of the plume cross section is small enough that the axisymmetric assumption still holds. This requires that the shear flow does not vary much on the length scale of an average plume radius. The three dimensional conservation equations (2)–(4) are rewritten to be in terms of length along the plume, s, instead of the depth z, as the depth of the plume locally now becomes a dependent variable. The plume's local radius is then defined relative to the center line. A new variable for the plume center line velocity $\hat{u}(s)$ is introduced, and the vertical momentum flux can then be written as $M = \frac{1}{2}b^2u\hat{u}$. The volume and buoyancy flux are also modified, as $Q = \pi b^2\hat{u}$ and $F = \lambda^2/(1+\lambda^2)\hat{u}b^2g\Delta\rho/\rho_0$ respectively. After also taking into account the density and velocity profile ratio λ, a system of five differential equations can then be written:

$$\frac{dQ}{ds} = 2\gamma b|\hat{u}|, \tag{15}$$

$$\frac{dM}{ds} = 2(1+\lambda^2)\frac{F}{\hat{u}}, \tag{16}$$

$$\frac{dF}{ds} = -ub^2N^2, \tag{17}$$

$$\frac{dz}{ds} = \frac{u}{\hat{u}}, \tag{18}$$

$$\frac{dx}{ds} = \frac{U_a}{\hat{u}}. \tag{19}$$

These equations are then completed by the Pythagorean theorem to relate the total velocity to the horizontal and vertical, $\hat{u}^2 = U_a^2 + u^2$, which assumes that the plume is advected by the horizontal velocity. The modified entrainment coefficient γ can be given as a weighted n-norm of the horizontal and vertical entrainments, with α and β as the horizontal and vertical entrainment coefficients respectively:

$$\gamma = \frac{1}{|\hat{u}|}\sqrt[n]{\alpha u^n + \beta U_a^n} \tag{20}$$

The horizontal advection assumption can be considered valid away from the initial flow establishment region of the plume, where the ambient velocity dominates any other turbulent horizontal velocities. Note that in the limit as $U_a \to 0$ the equations reduce to the simple three-ODE system in equations (2)–(4).

2.2. Zone of flow establishment

The initial cross-sectional velocity and density profiles when the plume leaves the discharge pipe are well approximated by tophat functions. An initial region exists, called the "zone of flow establishment", where self-similarity has not yet developed and the velocity profile undergoes large changes. After between 4-to-8 pipe diameters the profile becomes approximately Gaussian and thereafter is self-similar, in what is called the "zone of established flow" (wei Lee and Chu, 2003). To account for the zone of flow establishment in the model, we use the results of Henderson-Sellers (1983). The initial tophat radius b_i, velocity u_i, and buoyancy g_i, when considered in the context of the initial Froude number $\mathrm{F_D} = u_i/\sqrt{g_i b_i}$, give the length of the zone of flow establishment as $f_z(F_D)$, where

$$f_z(\mathrm{F_D}) = \begin{cases} 8b_i & \mathrm{F_D^2} < 8 \\ (6.54 - 0.52\mathrm{F_D})b_i & 8 \le \mathrm{F_D^2} \le 128 \\ 12.4b_i & \mathrm{F_D^2} > 128. \end{cases} \tag{21}$$

Since this distance in never more than 14 times the initial pipe radius, crossflows are ignored over this small region to simplify the calculations. The new effective starting position of the plume, based on the physical depth of the pipe exit z_i, is therefore

$$z_e = z_i + f_z(F_D). \tag{22}$$

The standard plume equations can then be started at this effective depth, assuming a gaussian cross section, with effective radius, velocity, and buoyancy b_g, u_g, g_g given by

$$b_g = \sqrt{2}\,b_a \tag{23}$$

$$u_g = u_i f_u(\mathrm{F_D}) \tag{24}$$

$$g_g = \frac{1+\lambda^2}{2\lambda^2 f_u(\mathrm{F_D})}g_i \tag{25}$$

where

$$f_u(\mathrm{F_D}) = \begin{cases} 1.66 & \mathrm{F_D^2} < 8 \\ 1.99 - 0.24\ln(\mathrm{F_D^2}/2) & 8 \le \mathrm{F_D^2} \le 128 \\ 1.00 & \mathrm{F_D^2} > 128. \end{cases} \tag{26}$$

2.3. Compressibility and thermodynamic considerations

For the most part, the original study of Morton et al. (1956) studied incompressible scenarios where the variations in density and temperature were small enough to allow for a linearized equation of state. Accounting for compressibility properly in the context of a reduced plume model requires careful thermodynamic considerations; these are presented in detail in Appendix A. To summarize, the main outcome for the plume model is the calculation of N^2 to a good approximation as

$$N^2 = \frac{g}{\rho_0}\frac{\partial \rho_a}{\partial z} - \frac{g^2}{\bar{c}^2}, \tag{27}$$

where $\bar{c}^2$ is the speed of sound in the ambient background. When salinity is constant the above reduces to the buoyancy frequency calculated via potential density.

Pressure variations must also be considered when inspecting the thermodynamics of the model. In general, the pressure term will be a sum of the hydrostatic and dynamic pressures,

Table 1
Parameters used in the model and typical values (Oebius et al., 2001; Rolinski et al., 2001; Becker et al., 2001; Poletto and Joseph, 1995; Hein and Koschinsky, 2014; Assembly of Engineering, U.S., 1975; Halbach et al., 1975; Nafe and Drake, 1963; wei Lee and Chu, 2003; Devenish et al., 2010; Matulka et al., 2014).

Parameter	Variable	Value
Process water flow rate	Q_w	0.56 m^3/s
Sediment discharge rate	$\dot{m}_s$	3.1 kg/s
Fines discharge rate	$\dot{m}_f$	1.54 kg/s
Particle concentration in discharge	$(Q_A + Q_{SK})/Q_w$	8.29 kg/m^3
Pipe diameter	b_i	0.25 m
Discharge depth	z_i	1000 m
Mean discharge velocity	$u_i = Q_w/(\pi b_i^2)$	2.85 m/s
Initial plume water surface density	ρ_i	1029.5 kg/m^3
Reference density	ρ_0	1024 kg/m^3
Sediment solid density	ρ_s	2680 kg/m^3
Sediment apparent density	ρ_{sa}	1300 kg/m^3
Fines solid density	ρ_f	3334 kg/m^3
Fines apparent density	ρ_{fa}	2000 kg/m^3
Seafloor Salinity	s_i	34.9 PSU
Sediment average particle diameter	d_s	0.63 mm
Sediment settling velocity	u_s	1.2 mm/s
Plume entrainment coefficient	α_p	0.088
Jet entrainment coefficient	α_j	0.057
Horizontal entrainment coefficient	β	0.5
Plume Froude number	Fr_p	4.5
Density-Velocity profile ratio	λ	1.19
Background Flow	U_a	0.1 m/s

$p(z, r, t) = \bar{p}(z) + p'(z, r, t)$, where $\bar{p}$ is hydrostatic and p' is dynamic. The dynamic pressure in turn is due to both the mean flow velocity $\bar{u}$ and any turbulent fluctuations u', giving a total flow velocity of $u = \bar{u} + u'$. The ratio of the velocity fluctuations to mean velocity gives the turbulence intensity $I = u'/\bar{u}$. For buoyant plumes, empirical results suggest a maximal turbulence intensity of 32% (Papanicolaou and List, 1988; Shabbir and George, 1994). For a plume with mean flow velocity $\bar{u} = 2.85$m/s this corresponds to maximal velocity fluctuations on the order of

$$u' = 0.91\text{m/s}, \tag{28}$$

with corresponding dynamic pressures fluctuations of

$$p' \approx \frac{1}{2}\rho_0 \bar{u}^2 = 0.072 \text{ Bar}. \tag{29}$$

From the result in equation (29), the dynamic pressures correspond to no more than 0.7 m in vertical hydrostatic variations. On the tens to hundred meters scale of the plume these variations are negligible, and thus it is safe to ignore dynamics pressure fluctuations compared to the hydrostatic background.

The significance of compressibility can be determined by a ratio of the two terms on the right of equation (27), encapsulated as the dimensionless number

$$\Theta = \frac{\bar{c}^2}{\rho_0 g}\frac{d\rho_a}{dz}. \tag{30}$$

$\Theta<1$ implies an unstable background that would not be observed and $\Theta= 1$ corresponds to a neutrally stable profile in which the change in ambient density is due to compressibility alone. If Θ modestly exceeds unity then compressibility plays an important role in the dynamics, while if $\Theta \gg 1$ then compressibility effects are negligible. Fig. 2(c) presents two data sets for Θ, one for a single ARGO profile and another for a 10 year summer average. In the shallow pycnocline layer, where there is a large temperature gradient, we see Θ values on the order of 5–10, meaning the density change is 80–90% due to temperature. Below the pycnocline, however, Θ is near but still greater than unity, meaning that density changes below about 600 m are due almost completely due to compressibility.

2.4. Environmental and plume parameters

Discharge plumes released into the ocean water column will experience a non-uniform stratification as they evolve downwards. We perform our case studies using a set of ARGO stratifications obtained from the Clarion-Clipperton Fracture Zone (CCFZ), the region southeast of the Hawaiian islands that is being actively considered for deep-sea nodule mining operations. We consider an average stratification taken from Roemmich and Gilson (2009) using a July average over the last 10 years, along with the stratification measured by a single ARGO profile in the Summer of 2016. Both of these were measured at 144 ± 1°W, 15 ± 1°S, near the center of the CCFZ. The reason for considering these two different types of profiles is to investigate the impact that small-scale features, which will be smoothed out in a time averaged profile, have on plume evolution. The stratification data is presented in Fig. 2(a) and (b), comprising a rapid increase in potential density with depth near the surface (the pycnocline) followed by a far slower increase of potential density with depth in the deeper water column. For the square of the buoyancy frequency N^2 the single measured profile has significantly greater variation in gradient than the averaged profile, as would be expected. Fig. 2(c) presents the value of Θ as a function of depth, illustrating that in the upper few hundred meters of the water column, where Θ attains a value as high as 12, compressibility effects are negligible, but at depths of 500 m or below the value of $\Theta \approx 1$, meaning compressibility effects will be significant.

In addition to the ambient density stratification, the ambient velocity profile also plays a role in the plume dynamics. Fig. 2(d) shows both single and averaged total absolute velocity profiles taken in the CCFZ. In the upper ocean the velocities are much higher, which can have a large effect on the plume. At lower ocean depths the velocities are found to be on the order of 0.02–0.05 m/s when averaged. Given that the available ADCP data only extend to a depth of about 800 m, the averaged velocities of the lower portion of the profile will be used to give a reasonable estimate of the expected magnitude of flows for even deeper releases.

For our case study, we utilize established reasonable parameters for nodule-mining discharge plumes (Oebius et al., 2001). The main waste products in such an operation will be sediment that has agglomerated on nodules, and fines from the nodules themselves. Parameter estimates for the resulting discharge plumes are 0.56 m^3/s for the waste water discharge, with 3.1 kg/s of sediment and 1.5 kg/s of fines created by abrasion of nodules. The postulated initial diameter of the plume, set by the pipe diameter, is 0.5 m. For a full list of parameters and their values, see Table 1; these are our baseline parameter values that we will use unless explicitly stated otherwise.

Based on theoretical and experimental results (wei Lee and Chu, 2003; Matulka et al., 2014), a variable entrainment coefficient of the form

$$\alpha = \alpha_j - (\alpha_j - \alpha_p)\left(\frac{\mathrm{Fr}_p}{\mathrm{Fr}}\right)^2 \tag{31}$$

is used to account for the transition from jet to plume in the discharge. Here α_j and α_p are the entrainment coefficient of a jet and plume respectively, Fr_p the Froude number of a pure plume, and $\mathrm{Fr} = u/\sqrt{g'b}$ the local Froude number. Values for the first three constants are noted in Table 1. The flow rate variables and initial plume geometry are taken from Oebius et al. (2001), while the mean sediment radius is taken from Becker et al. (2001). An average background flow of 0.1 m/s is assumed due to both ship movement and background current (this is taken as a likely lower bound). In most operating conditions it is likely that some ambient velocity will be present, hence the choice to assume the average plume is being released into some background current. To find

the density of nodule fines we use Halbach et al. (1975), while the density of the sediments is taken from Nafe and Drake (1963). We assume Stokes drag to calculate the settling velocity of the sediment, and use the apparent density to account for pores, which is about 1300 kg/m^3 for sediment and 2000 kg/m^3 for fines. It is also assumed that the discharge plume has the same salinity as deep ocean water, taken here as the salinity at 1900m measured in the ARGO soundings and climatology.

To calculate the initial density of the plume we consider the plume a multiphase fluid of density

$$\rho_i = \frac{\sum \dot{m}_n}{\sum Q_n}, \tag{32}$$

where $\dot{m}_n$ are mass flow rates and Q_n are volume flowrates of each phase. Noting that for each component $\rho_n = \dot{m}_n/Q_n$ we can recast the right side of equation (32) using known quantities to obtain

$$\rho_i = \frac{\dot{m}_s + \dot{m}_f + \rho_w Q_w}{\dot{m}_s/\rho_s + \dot{m}_f/\rho_f + Q_w}, \tag{33}$$

where ρ_s, ρ_f and ρ_w are the sediment, fine, and water density respectively, $\dot{m}_s$ and $\dot{m}_f$ are sediment and fine mass flow rates, and Q_w is the water volume flow rate. Utilizing the density of the water calculated using the equation of state in Gibbs Seawater Oceanographic Toolbox (McDougall and Barker, 2011), one can determine the net starting density of the plume and therefore the initial buoyancy flux.

The appropriate Reynolds number in the return pipe, calculated using the data listed in Table 1, is

$$\mathrm{Re} = \frac{ud\rho}{\mu} \approx 1.6 \times 10^6. \tag{34}$$

Given that the return pipe will be many times longer than it is wide, the exit flow will be well-developed turbulent pipe flow, and the resulting plume will also be highly turbulent. The discharge velocity ($u_i \approx 2.85$ m/s) is far greater that the mm/s settling speeds of the particles, or even cm/s settling speeds of coagulated particles, and so we can expect the majority of particles to stay in suspension until the plume is close to coming to rest. Some particles may precipitate out of the plume at its side boundaries with the ambient, where the flow is relatively slow, but particle concentrations will be low here due to turbulent entrainment and so we expect this to be a second order effect that the current model doesn't address. The slip velocity of the sediment particles is low enough to ignore the multiphase nature of the flow (Wang and Adams, 2016).

2.5. Practical pipe flow considerations

The discharge water has several potential origins and changes of characteristics throughout the processing. It may be drawn up from the ocean floor with the nodules or from near the ocean surface to facilitate the on-board processing, and most likely some combination of both. And throughout the riser transport and on-board processing the water temperature may change appreciably due to the origin of the water, transport through a vertically varying background environment, and heating or cooling during the surface ship processing. All of such practical considerations must be taken into account when determining the initial density (and thus buoyancy) of the discharge plume.

We use the methods of Incropera et al. (2007) to estimate the change in temperature of water in the discharge pipe as it is pumped from the surface processing vessel to the release depth. Assuming an averaged fluid temperature $T(z)$ for a cross section of the pipe, the equation governing temperature evolution within the pipe is:

$$\frac{dT}{dz} = \frac{2\pi b}{\rho_w Q_w c_p} h(T_a - T), \tag{35}$$

where c_p is the specific heat of the water, $T_a(z)$ the ambient water temperature, and h a heat transfer coefficient defined below. Note this equation only takes into account the thermal properties of the water and not the suspended particulate, as the temperature error due to the suspended mass is of the same order as the other errors inherent in our approximation. The thermal mass of the pipe is assumed to be negligible and its temperature to be identical to the surrounding ambient ocean. The parameter h is given by:

$$h = \frac{\mathrm{Nu}\, k_w}{2b}, \tag{36}$$

where k_w is the thermal conductivity of water and the Nusselt number is (Incropera et al., 2007):

$$\mathrm{Nu} = \frac{(f_p/8)(\mathrm{Re}-1000)\mathrm{Pr}}{1 + 12.7(f_p/8)^{1/2}(\mathrm{Pr}^{2/3} - 1)}, \tag{37}$$

where $\mathrm{Pr} = \mu c_p/k_w$ is the Prandtl number and f_p is the friction factor that is determined from a moody diagram for a smooth tube with a turbulent flow to be

$$f_p = 0.184\mathrm{Re}^{-1/5}. \tag{38}$$

From the above, we can define a decay length scale μ for the temperature deviation:

$$\mu = \frac{\rho_w Q_w c_p}{2\pi h b} \approx 200\mathrm{m}. \tag{39}$$

It is thus evident that the outlet temperature will likely not be close to either the inflow temperature T or the ambient temperature at release, at least in the upper ocean where significant background temperature changes occur over lengthscales of 200 m. This requires full solution of equation (35) to find the correct outflow temperature, and thus outflow density.

A schematic of how heat transfer enters into the solution process is presented in Fig. 3. The initial data includes the ambient temperature and salinity profiles, taken from individual ARGO profiles or the averaged climatology, along with flow data and other engineering parameters. Unless otherwise noted, for this paper we use the surface temperature as T_i, along with the salinity at the deepest measured point on the profile for S_i. The heat transfer differential equation (35) is used to determine how the temperature of this water changes as it travels down from the surface to the release depth. The final temperature of this calculation is considered to be the initial temperature of the discharge plume. Along with the initial salinity, which we assume does not change in the travel from the surface to release depth, we use the Gibbs Seawater Toolbox to calculate the plume initial density. This, along with the initial flow rate, plume radius, and other physical parameters allows calculations of the initial momentum and buoyancy flux. This is then enough data to calculate the extent and effects of the zone of flow establishment on the initial parameters using equations (21)-(26). Finally, the modified initial data for the zone of established flow lets us solve for the plume profile using equations (15)-(19).

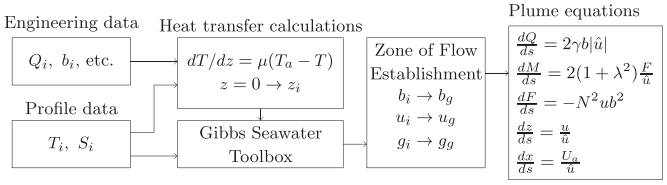


Fig. 3. Schematic of the solution process for the plume calculation. Initial data is fed through heat transfer, equation of state, and flow establishment calculations before being used in the plume equations.

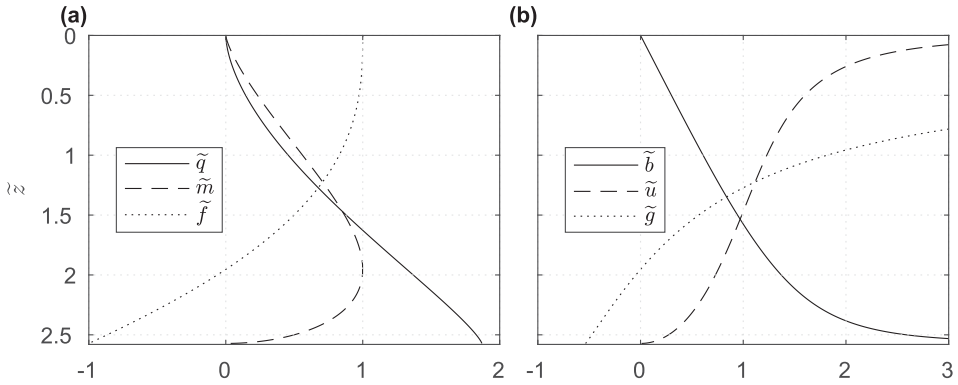


Fig. 4. Non-dimensional solution for a plume with a uniform stratification. (a) Non-dimensional flowrate $\tilde{q}$, momentum flux $\tilde{m}$, and buoyancy flux $\tilde{f}$ as a function of depth. (b) Non-dimensional radius $\tilde{b}$, velocity $\tilde{u}$, and buoyancy $\tilde{g}$ as a function of depth.

3. Results

3.1. Uniform stratification results

We first consider a plume release in a uniform stratification, zero ambient velocity, and with zero initial momentum or volume flux, reproducing the classic non-dimensional solution for a point plume in a stratified ambient (Morton et al., 1956). For this we use equations (9)-(11) as our system of ODEs to solve, with zero initial volume and momentum flux conditions, i.e. $\tilde{q}(0) = \tilde{m}(0) = 0$. From our nonlinearization, we set the initial dimensionless buoyancy flux to be unity, $\tilde{f}(0) = 1$, and the corresponding results are presented in Fig. 4(a). We then use equations (12)-(14) to convert these results into non-dimensional radius $\tilde{b}$, velocity $\tilde{u}$, and buoyancy $\tilde{g}$, and plot the corresponding results in Fig. 4(b). The latter two variables rapidly decrease over an initial distance, and then slow their decrease in what we can consider the established region of the plume, with the velocity going to zero and the buoyancy changing sign, indicating an upward rebound will occur when the momentum flux reaches zero. The radius on the other hand increases at roughly the same rate for most of the plume's length, except near its end at which point it rapidly increases to become infinite as the plume terminates. These values match what is expected for a plume in a uniform stratification, confirming our implementation.

In solving equations (9)-(11) for a (non-dimensional) plume in a stratified ambient, as in Morton et al. (1956) we assume the plume to be a buoyancy point source with zero initial flowrate $\tilde{q}_i$ and radius $\tilde{b}_i$. We varied the values of these latter two parameters and studied their influence on the non-dimensional length of the plume $\tilde{l}$, with the results being presented in Fig. 5(a). A notable feature of the results is the non-monotonic behavior of the plume length as a function of flow rate, as previously reported by Fox (1970), this being particularly noticeable for small initial radii. The rationale for the non-monotonic behavior is as follows. For low flowrates a plume is buoyancy dominated while at high flowrate it is momentum dominated. Increasing the flowrate for a buoyancy dominated plume acts to increase mixing, entraining more ambient fluid near the plume source and decreasing the density anomaly, which inhibits downward transport. On the other hand, a momentum dominated plume increases in length with increasing flowrate due to the extra momentum provided. When these two effects are balanced the plume attains its minimum length. For larger radii, the turn-around point happens at a larger flowrates due to the increased dominance of buoyancy compared to momentum. Fig. 5(b) presents the corresponding dimensional results (using the information in Table 1 for all non-varying parameters, with zero ambient velocity) to show how this effect is even more evident when presented in dimensional form; this is due to the dependence of the dimensional depth z on $F_0^{1/4}$ as given in equation (5). As F_0 increases with Q_i, all other things equal, this results in a pronounced increase of L with Q_i in the dimensional compared to the non-dimensional case.

3.2. Non-uniform stratification results

We next consider a discharge plume released into the ambient stratifications presented in Fig. 2(a), along with a constant ambient crossflow of 0.1 m/s. First, we use the parameter values listed in Table 1 and the solution procedure outlined in Fig. 4; the results are presented in Fig. 6. For these standard values, the compressible plume has a vertical extent of about 190 m and a final width of about 35 m. The presence of a background ambient flow prevents a runaway growth in plume radius (compared to the non-dimensional zero ambient velocity case), while the mean turbulent velocity and density anomaly both initially rapidly decrease and thereafter evolve at a much slower rate for the majority of the remaining extent of the plume. The vertical velocity decelerates to zero at the base of the plume, while the final density anomaly is approximately $-0.027\ kg/m^3$, which corresponds to a dilution factor of about 300; the level of neutral buoyancy of the final density of the plume is about 150 m below release. The qualitative shape of the plume shows a much more gradual increase in radius compared to Fig. 4(b), largely due to the presence of an ambient velocity profile. On the other hand, the velocity and density anomaly curves are qualitatively very similar to the non-dimensional case, even though the compressibility-modified density gradient varies by as much as 30% over the length of the plume (0.6–0.4 kg/m^4). For the majority of the plume's length, the magnitude of the vertical (turbulent) velocity shown in Fig. 6(b) is orders of magnitude larger than the expected sediment settling velocity for either individual or coalesced particles (Becker et al., 2001); thus we can be confident in our modeling assumption that the particulate acts as a passive tracer up until the end of the plume.

The reference values in Table 1 can be varied independently to investigate their effect on the plume. We start by investigating the influence of the initial downward buoyancy flux, F_0, and flow rate, Q_0, and plot the resulting vertical extent L in Fig. 7(a) and (b), respectively, for both a 10 cm/s ambient velocity and a quiescent background. As expected, the increase in initial buoyancy causes a monotonic increase in the vertical extent in Fig. 7(a). In varying the flow rate (Fig. 7(b)), for a quiescent background we see the same non-monotonic behavior that is present in the uniform stratification case in Fig. 5, while for the 10 cm/s ambient case the plume length is always increasing. This change of form can be explained by the dependence of heat transport in the pipe on the ambient crossflow rate, combined with increased entrainment after plume ejection. At low ambient flow rates, the convective heat transfer away from the pipe due to the ambient velocity is minimal. This means that the plume length vs. flowrate for a given pipe diameter acts the same way as Fig. 5, with a local minimum in length vs. flowrate. A strong crossflow, however, causes large convective cooling of the pipe, bringing the exit temperature of the pipe close to the ambient. This decreases the effective buoyancy of the plume. Besides the

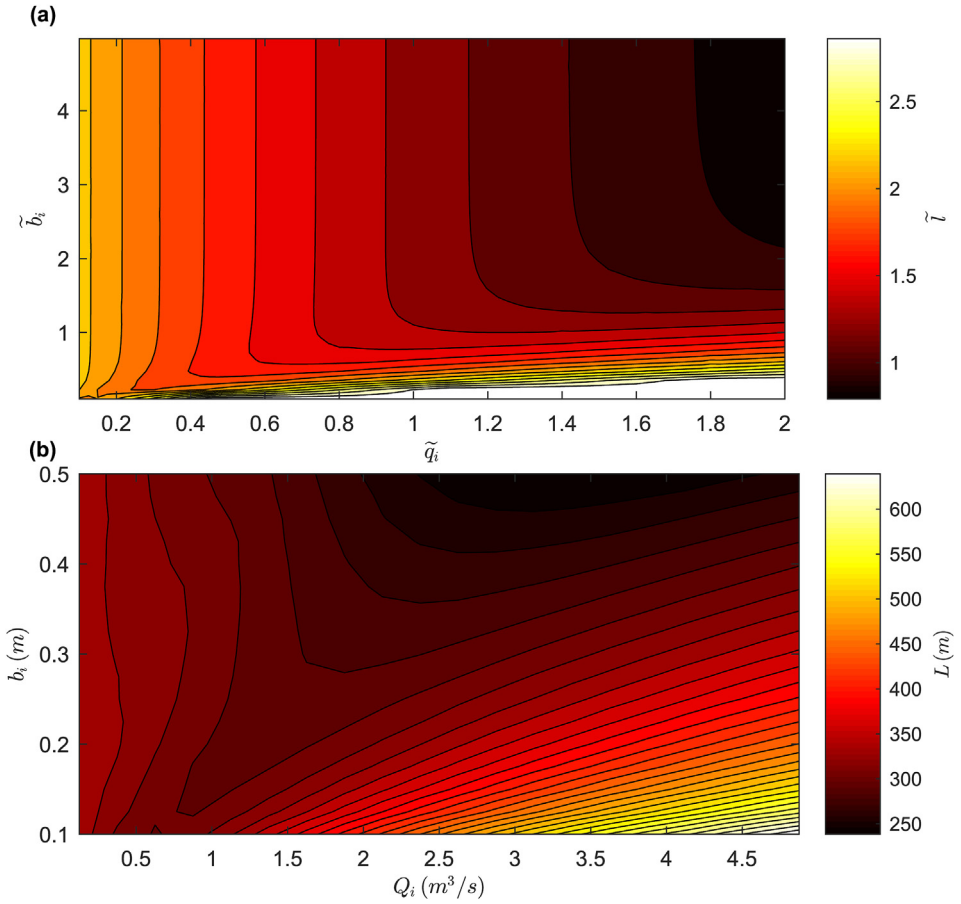


Fig. 5. Plots of plume vertical extent compared to initial flow rate and radius for a uniform stratification. In (a) we present dimensionless flowrate $\tilde{q}_i$ and radius $\tilde{b}_i$ for a non-dimensionalized plume with uniform stratification, while in (b) we present a plume with parameters as in Table 1, while varying the dimensional flow rate Q_i and radius b_i.

buoyancy effect due to temperature, the increased entrainment due to a stronger crossflow tends to eliminate any remaining buoyancy anomily more rapidly. The combined effect of these two mechanisms means that the momentum flux is the primary driver of plume length in a strong crossflow, which removes the local minimum in plume length vs. flow rate, instead making it a monotonically increasing function.

A parameter of that is inevitably of great importance in determining the vertical extent and final intrusion depth of a plume is the release depth, since this impacts the local background stratification and ambient velocity experienced by the plume as well as the contribution of heat transfer in the return pipe. Keeping all other parameters constant as given in Table 1 (with a constant background velocity of 0.1 m/s), the resulting plot of plume vertical extent vs. release depth is presented in Fig. 8, for both measured and averaged profiles. In both cases, a plume released in the upper ocean has its extent decrease with depth until below the thermocline, thus creating a local minimum in extent vs release depth. As the release depth goes below the thermocline there is a notable increase in plume extent, due to the

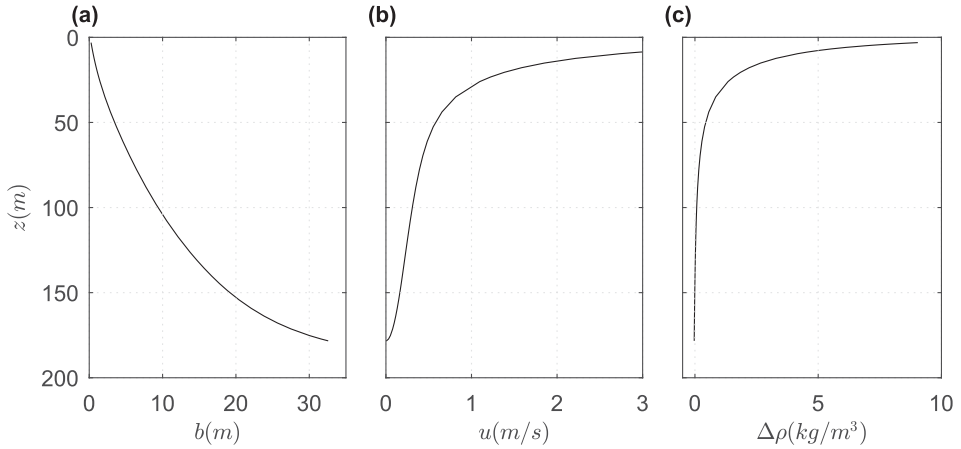


Fig. 6. Dimensional solution for a plume with parameters given in Table 1. We show, as a function of distance from plume start, (a) plume radius b, (b) plume characteristic turbulent velocity u, and (c) plume density anomaly $\Delta\rho_\theta$.

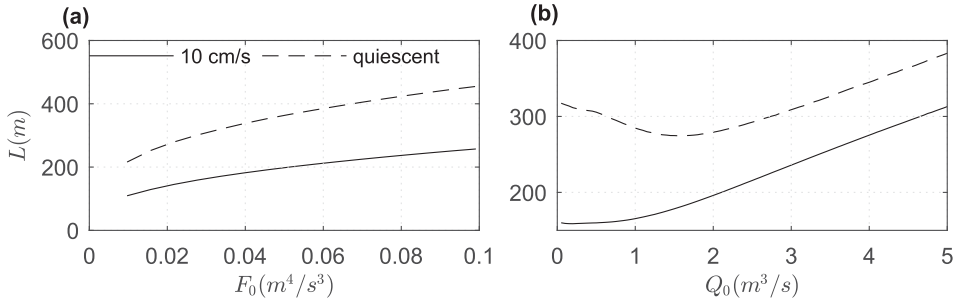


Fig. 7. Plume vertical extent L as a function of (a) initial buoyancy flux F_0 and (b) the initial volume flux Q_0, both for quiescent and 10 cm/s ambients.

stratification gradient asymptotically approaching zero. The curve corresponding to the single measured profile has greater small-scale variability compared to the averaged climatology results. Fig. 8 also presents results that do not account for heat transfer effects in the return pipe. For shallow releases the time available for heat transfer in the pipe is minimal and so there is little impact, but as the release depth increases heat transfer effects become more significant, and failure to take them into account results in significant underestimation of the plume length.

For environmental planning, it is also of interest to consider how plume traits other than just the plume length vary with respect to the release depth. In Fig. 9 we plot the plume's characteristic turbulent velocity u_f at 90% of the plumes length, particulate density ρ_{pf} (determined by dividing the initial particle mass flux by the final plume volume flux), and diameter d_f. The turbulent plume velocities in Fig. 9(a) and particulate densities in Fig. 9(b) are highest in the upper ocean and drop off rapidly for lower plumes, becoming more or less constant after a release depth of about 500 m. The turbulent plume velocities are all at least an order of magnitude above sediment settling velocities, consistent with our assumption that sedimentation is not important until the end of the plume. One can calculate the dilution of the sediment from release to plume end using the densities in Fig. 9(b) and the initial suspension densities in Table 1. In the worst case scenario, a release in the upper ocean near the surface can result in a plume with a dilution factor of less than 3 before termination. On the other hand, a release below 500 m in depth results in final dilution factors between 500 and 800.

Given the large effects that relatively small changes in ambient velocity have been shown in Fig. 7, it is worth investigating the influence of ambient velocity on plume length and dilution factor. The results are presented in Fig. 10(a). A velocity of 10 cm/s reduces a plume's depth by 50% compared to stagnant ambient, while a half meter per second reduces it by 75%. The dilution factor of the plume increases with cross flow velocity at low speeds, while decreasing at high speeds. The increase at low speeds is expected as the cross flow increases entrainment into the plume. At high ambient velocities however the time for the plume to reach its final depth is greatly decreased, giving less time for entrainment and thus less dilution when the plume reaches its final depth.

As a final, take-away result that is representative of what might be expected in the CCFZ, we consider plume releases at varying depths in the stratification and velocity profiles presented in Fig. 2. Fig. 11(a) presents plume extents vs. release depths based on both the single and averaged CCFZ shear profile found in Fig. 2(a). For a deep release, the background velocities are on the order of 2 cm/s, which have negligible impact on the plume length. A shallow release, however, encounters velocities as high as 18 cm/s, which reduces the length of the plume to almost a third of the stagnant ambient length. Corresponding dilution factors of 50–250 are presented in Fig. 2(b), becoming significantly higher for a deeper release that allows longer plumes and greater entrainment. The model also predicts quite different plume lengths and dilution factors for the single and averaged CCFZ shear profiles, emphasizing the impact of small-scale features in the stratification and

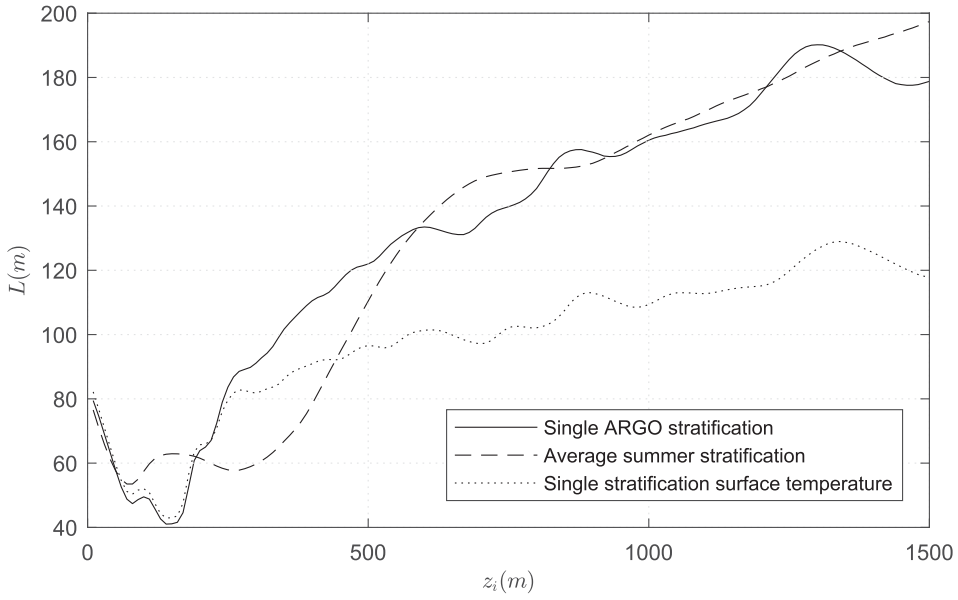


Fig. 8. Plume vertical extent L as a function of release depth z_i. The solid and dashed curves are for a single measured stratification and an average stratification, respectively, both taking into account heat transfer as the plume descends. The dotted curve uses the single measured stratification but assumes no heat transfer in the return pipe, meaning the initial plume outlet temperature matches the measured surface temperature.

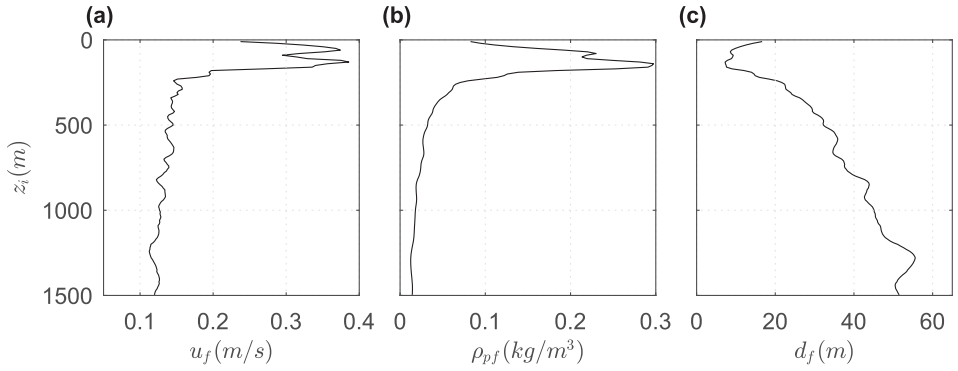


Fig. 9. Plume end parameters as a function of release depth z_i. (a) final mean velocity u_f (b) final particulate density ρ_{pf} and (c) final plume diameter d_f.

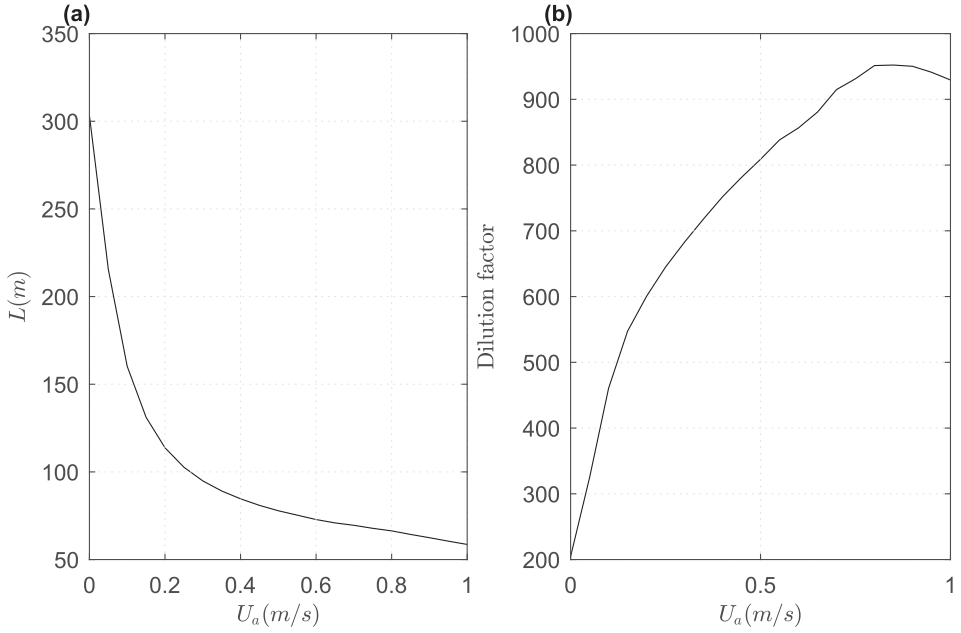


Fig. 10. Plume end parameters as a function of constant ambient background velocity, for a 1000 m depth release with standard parameters. (a) Plume length, and (b) dilution factor.

vertical shear.

4. Discussion

In this paper, we studied the potential form of deep-sea nodule mining discharge plumes in the context of classic plume theory. Our approach used the classic equations of plume theory with arbitrary varying stratification, augmented with compressibility and thermal conduction through the return pipe walls. Initial conditions for the plume are vital for determining the nature of the subsequent plume evolution, and changing important engineering parameters make it possible to drastically affect the length and dilution factor of the resultant plume. Our studies also demonstrated the importance of accurate local stratification and vertical shear data in determining the plume evolution.

For a characteristic CCFZ stratification, a discharge plume will have a length on the order of 100 m, with a dilution factor of between 100 and 1000; background sediment concentrations will be on the order of 0.1–0.01 kg/m^3 and corresponding volume fractions will be between 10^{-4} or 10^{-5}. In addition to monitoring background stratification and crossflows, mining operations will have to perform careful heat budgets as the decay length of the temperature in the return pipe is on the order of the plume length.

This model provides a first-order approach for calculating the properties of discharge plumes to be input as source conditions for regional scale ocean models. In taking into account the expected stratifications and crossflows, the variable final depth of the plume becomes a variable initial depth of a sediment source for a regional model. This variation in turn gives a truer picture of final sediment fate as compared to a fixed source depth. The plume model also provides a bridge to couple the variation of local engineering parameters to the environmental impacts in the larger regional scale model.

These studies did not model plume rebound, which would likely have to take into account the multi-phase nature of the suspended particles. At the arrest of a plume, where turbulent velocities vanish, sediment fallout is likely, and this in turn will likely impact the rebound height due to a significant effective change in density. With heavier particles leaving the flow, this would allow for larger rebounds than for a single-phase case. The fallout of sediment from the sidewalls of the plume could also be of environmental interest given the long times for which these plumes will be running. All of these effects combine to decrease the total plume length, meaning that the single-phase model gives an upper bound to the total plume and rebound depths.

Declarations of interest

None.

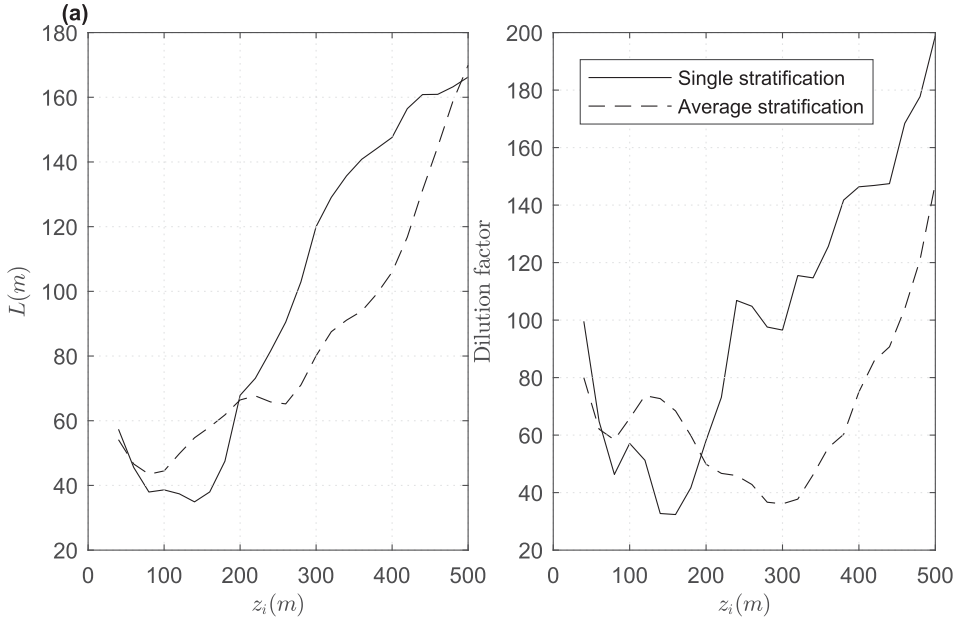


Fig. 11. (a) Plume extent vs. release depth with measured CCFZ background shear. Single vs. averaged shear profiles show large differences in extent, though both are increasing on average with release depth. (b) Plume dilution factor as a function of release depth with CCFZ background shear.

Acknowledgements

These data were collected and made freely available by the International Argo Program and the national programs that contribute to it. (http://www.argo.ucsd.edu, http://argo.jcommops.org). The Argo Program is part of the Global Ocean Observing System. This work was supported by NSF grant DMS-1318942, the Hertz Foundation and an MIT Environmental Solutions Initiative seed grant.

Appendix A. Derivation of plume equations for compressible flow

A detailed derivation of the plume equations (2)–(4) is herein considered, accounting for compressibility and salinity. We start with a basic set of conservation equations in vector form. Here $\mathbf{u}$ is the fluid velocity, and the z direction is taken as positive downward (in the same direction as gravity). Conservation of mass states, for density ρ,

$$\frac{\partial \rho}{\partial t} + \nabla\cdot(\rho\mathbf{u}) = 0 \tag{A.1}$$

Both density and pressure can be written as a mean background field plus a deviation, as $\rho = \bar{\rho}(z) + \rho'$ and $p = \bar{p}(z) + p'$, respectively. The background pressure is related to the background density through the hydrostatic relation

$$\frac{\partial}{\partial z}\bar{p} = \bar{\rho}g \tag{A.2}$$

Next, vertical momentum conservation for an inviscid fluid, with u taken as the vertical velocity component, is written

$$\frac{\partial}{\partial t}(\rho u) + \nabla\cdot(\rho u\mathbf{u}) = g\rho' - \frac{\partial p'}{\partial z}. \tag{A.3}$$

We define reduced gravity as

$$g' = g\frac{\bar{\rho} - \rho}{\rho} \tag{A.4}$$

and then rewrite the momentum equation by plugging in (A.4) into (A.3) to get

$$\frac{\partial}{\partial t}(\rho u) + \nabla\cdot(\rho u\mathbf{u}) = g'\rho - \frac{\partial}{\partial z}p', \tag{A.5}$$

We write the thermodynamic equation in density/pressure form as in Vallis (2006), noting that with the lack of source and diffusion terms the equation becomes

$$\frac{D}{Dt}\rho = \frac{1}{c^2}\frac{D}{Dt}p, \tag{A.6}$$

where c can be taken as a function of density, salinity, and pressure. Substituting in the hydrostatic relation (A.2) gives:

$$\frac{D}{Dt}\rho = \frac{1}{c^2}\left(ug\bar{\rho} + \frac{D}{Dt}p'\right). \tag{A.7}$$

A conservation equation for reduced gravity can then be written by first using the product rule on the derivative of $\rho g'$ to write

$$\frac{D}{Dt}(\rho g') = \rho\frac{D}{Dt}g' + g'\frac{D}{Dt}\rho; \tag{A.8}$$

and then substituting the reduced gravity (A.4) for the left term gives

$$g\frac{D}{Dt}(\bar{\rho} - \rho) = \rho\frac{D}{Dt}g' + g'\frac{D}{Dt}\rho; \tag{A.9}$$

Solving equation (A.9) for the $\rho\frac{D}{Dt}g'$ and substituting the density conservation equation (A.7) and the hydrostatic relation (A.2) gives (after noting that $g + g' = g\bar{\rho}/\rho$):

$$\rho\frac{D}{Dt}g' = ug\frac{\partial\bar{\rho}}{\partial z} - u\bar{\rho}\frac{g^2}{\bar{c}^2} + u\bar{\rho}\left(\frac{g^2}{\bar{c}^2} - \frac{\bar{\rho}}{\rho}\frac{g^2}{c^2}\right) - \frac{g}{c^2}\frac{\bar{\rho}}{\rho}\frac{D}{Dt}p'. \tag{A.10}$$

From the above equation (A.10) we define a background buoyancy frequency using

$$\bar{N}^2 = \frac{g}{\bar{\rho}}\frac{\partial\bar{\rho}}{\partial z} - \frac{g^2}{\bar{c}^2} \tag{A.11}$$

The right side of equation (A.10) can now be rewritten using (A.11), and the left side put into the conservative form, as

$$\frac{\partial}{\partial t}(\rho g') + \nabla\cdot(\rho g'\mathbf{u}) = \bar{\rho}u\bar{N}^2 + \bar{\rho}u\left(\frac{g^2}{\bar{c}^2} - \frac{g^2}{c^2}\right) + \bar{\rho}u\frac{gg'}{c^2} - \frac{g}{c^2}\frac{\bar{\rho}}{\rho}\frac{D}{Dt}p' \tag{A.12}$$

Before moving forward, it is worth comparing the terms on the right side of equation (A.12) to allow for possible simplifications. First, note that in the regime that the plume here will be considered $\bar{c} \approx c$ over the range of temperatures and salinity considered, resulting in

$$\bar{N}^2 \gg \left(\frac{g^2}{\bar{c}^2} - \frac{g^2}{c^2}\right), \tag{A.13}$$

allowing the second term on the right of (A.12) to be neglected. Furthermore, as $g' \ll g$, this also gives

$$\bar{N}^2 \gg \frac{gg'}{c^2}, \tag{A.14}$$

and allows the third term to also be neglected. Finally, the last term on the right of (A.12) due to pressure variations can be neglected as they are small and the plume equations will be taken to be in steady state. The p' term in (A.5) can be neglected for the same reason.

With these approximations, we are left with a system of three partial differential equations, based on equations (A.1), (A.5), and the simplification of (A.12):

$$\frac{\partial\rho}{\partial t} + \nabla\cdot(\rho\mathbf{u}) = 0, \tag{A.15}$$

$$\frac{\partial}{\partial t}(\rho u) + \nabla\cdot(\rho u\mathbf{u}) = g'\rho, \tag{A.16}$$

$$\frac{\partial}{\partial t}(\rho g') + \nabla\cdot(\rho g'\mathbf{u}) = \bar{\rho}u\bar{N}^2. \tag{A.17}$$

The anelastic approximation would replace the ρ factors by $\bar{\rho}$; proceeding in the usual way leads to a closed set for the mass, momentum, and buoyancy. If we go one step further and replace ρ with ρ_0, then make the tophat approximation (wei Lee and Chu, 2003), we recover the equations (2)–(4) with the fully compressible definition of N^2.

The above derivation did not include the effect of a gaussian profile or of a ratio λ between the velocity and buoyancy radial extents. These and other additional modifications can be made following the methods in wei Lee and Chu (2003) applied to the modified conservation steady state equations (A.15)-(A.17).

References

Assembly of Engineering (U.S.), 1975. Panel on operational safety in marine mining. In: Mining in the Outer Continental Shelf and in the Deep Ocean. National Academy of Sciences, Washington.

Becker, H.J., Grupe, B., Oebius, H.U., Liu, F., 2001. The behaviour of deep-sea sediments under the impact of nodule mining processes. Deep Sea Res. Part II Top. Stud. Oceanogr. 48, 3609–3627.

Boschen, R., Rowden, A., Clark, M., Gardner, J., 2013. Mining of deep-sea seafloor massive sulfides: a review of the deposits, their benthic communities, impacts from mining, regulatory frameworks and management strategies. Ocean Coast Manag. 84, 54–67.

Burns, R.E., 1980. Assessment of environmental effects of deep ocean mining of manganese nodules. Helgol. Meeresunters. 33, 433–442.

Bush, J.W.M., Thurber, B.A., Blanchette, F., 2003. Particle clouds in homogeneous and stratified environments. J. Fluid Mech. 489, 29–54.

Camassa, R., Lin, Z., McLaughlin, R.M., Mertens, K., Tzou, C., Walsh, J., White, B., 2016. Optimal mixing of buoyant jets and plumes in stratified fluids: theory and experiments. J. Fluid Mech. 790, 71–103.

Caulfield, C.P., Woods, A.W., 1998. Turbulent gravitational convection from a point source in a non-uniformly stratified environment. J. Fluid Mech. 360, 229–248.

Collins, P.C., Croot, P., Carlsson, J., Colaço, A., Grehan, A., Hyeong, K., Kennedy, R., Mohn, C., Smith, S., Yamamoto, H., Rowden, A., 2013. A primer for the environmental impact assessment of mining at seafloor massive sulfide deposits. Mar. Pol. 42, 198–209.

Devenish, B.J., Rooney, G.G., Webster, H.N., Thomson, D.J., 2010. The entrainment rate for buoyant plumes in a crossflow. Bound-Lay. Meteorol. 134, 411–439.

Droppo, I.G., 2006. Suspended sediment transport flocculation and particle characteristics. In: Encyclopedia of Hydrological Sciences. John Wiley & Sons, Ltd.

Fischer, H., List, J., Koh, C., Imberger, J., Brooks, N., 1979. Mixing in Inland and Coastal Waters. Academic Press.

Fox, D.G., 1970. Forced plume in a stratified fluid. J. Geophys. Res. 75, 6818–6835.

Halbach, P., Ozkara, M., Hense, J., 1975. The influence of metal content on the physical and mineralogical properties of pelagic manganese nodules. Miner. Depos. 10, 397–411.

Hein, J., Koschinsky, A., 2014. Treatise: on Geochemistry. Chapter 11: Deep-ocean Ferromanganese Crusts and Nodules, vol 13. Elsevier, pp. 273–291.

Henderson-Sellers, B., 1983. The zone of flow establishment for plumes with significant buoyancy. Appl. Math. Model. 7, 395–398.

Hunt, G.R., van den Bremer, T.S., 2010. Classical plume theory: 1937-2010 and beyond. IMA J. Appl. Math. 76, 424–448.

Hunt, G.R., Kaye, N.B., 2005. Lazy plumes. J. Fluid Mech. 533, 329–338.

Incropera, F., DeWitt, D., Bergman, T., Lavine, A., 2007. Fundamentals of Heat and Mass

Transfer. Fundamentals of Heat and Mass Transfer. John Wiley, Hoboken, NJ.
Kaye, N.B., 2008. Turbulent plumes in stratified environments: a review of recent work. Atmos.-Ocean 46, 433–441.
Lavelle, J., Ozturgut, E., Baker, E., Swift, S., 1982. Discharge and surface plume measurements during manganese nodule mining tests in the north equatorial pacific. Mar. Environ. Res. 7, 51–70.
List, E.J., 1982. Turbulent jets and plumes. Ann. Rev. Fluid Mech. 14, 189–212.
Matulka, A., López, P., Redondo, J.M., Tarquis, A., 2014. On the entrainment coefficient in a forced plume: quantitative effects of source parameters. Nonlinear Proc. Geoph. 21, 269–278.
McDougall, T., Barker, P., 2011. Getting Started with TEOS-10 and the Gibbs Seawater (GSW) Oceanographic Toolbox. SCOR/IAPSO WG127.
Mehaddi, R., Candelier, F., Vauquelin, O., 2013. Naturally bounded plumes. J. Fluid Mech. 717, 472–483.
Morton, B.R., 1958. Forced plumes. J. Fluid Mech. 5, 151–163.
Morton, B.R., Middleton, J., 2006. Scale diagrams for forced plumes. J. Fluid Mech. 58, 165–176.
Morton, B.R., Taylor, G., Turner, J.S., 1956. Turbulent gravitational convection from maintained and instantaneous sources. Proc. R. of Lond. A: Math. Phys. Eng. Sci. 234, 1–23.
Nafe, J., Drake, C., 1963. Physical Properties of Marine Sediments. Chapter V. 3. New York Interscience, New York, pp. 784–815.
Nawab, Z., Luck, K., 1979. Test mining of metalliferous mud from the red sea bottom. Meerestechnik mt 10, 81–187.
Oebius, H.U., Becker, H.J., Rolinski, S., Jankowski, J.A., 2001. Parametrization and evaluation of marine environmental impacts produced by deep-sea manganese nodule mining. Deep Sea Res. Part II Top. Stud. Oceanogr. 48, 3453–3467.
Papanicolaou, P.N., List, E.J., 1988. Investigations of round vertical turbulent buoyant jets. J. Fluid Mech. 195, 341391.
Poletto, M., Joseph, D.D., 1995. Effective density and viscosity of a suspension. J. Rheol. 39, 323–343.
Roemmich, D., Gilson, J., 2009. The 2004-2008 mean and annual cycle of temperature, salinity, and steric height in the global ocean from the argo program. Prog. Oceanogr. 82, 81–100.
Rolinski, S., Segschneider, J., Sndermann, J., 2001. Long-term propagation of tailings from deep-sea mining under variable conditions by means of numerical simulations. Deep Sea Res. Part II Top. Stud. Oceanogr. 48, 3469–3485.
Santo, H., Hu, P., Agarwal, B., Placidi, M., Zhou, J., 2013. A proposed concept design solution towards full-scale manganese nodule recovery. In: ASME. International Conference on Offshore Mechanics and Arctic Engineering, Volume 3: Materials Technology. Ocean Space Utilization.
Schriever, G., Thiel, H., 2013. Tailings and their disposal in deep-sea mining. In: International Society of Offshore and Polar Engineers.
Segschneider, J., Sndermann, J., 1998. Simulating large scale transport of suspended matter. J. Mar. Syst. 14, 81–97.
Shabbir, A., George, W.K., 1994. Experiments on a round turbulent buoyant plume. J. Fluid Mech. 275, 132.
Socolofsky, S.A., Adams, E.E., 2002. Multi-phase plumes in uniform and stratified crossflow. J. Hydraul. Res. 40, 661–672.
Vallis, G.K., 2006. Atmospheric and Oceanic Fluid Dynamics. Cambridge University Press, Cambridge, UK.
Wang, D., Adams, E.E., 2016. Intrusion dynamics of particle plumes in stratified water with weak crossflow: application to deep ocean blowouts. J. Geophys. Res. Oceans 121, 3820–3835.
wei Lee, J.H., Chu, V., 2003. Turbulent Jets and Plumes a Lagrangian Approach. Springer.
Woods, A.W., 2010. Turbulent plumes in nature. Annu. Rev. Fluid Mech. 42, 391–412.